nature communications

Article

https://doi.org/10.1038/s41467-025-58922-z

Tunable magnons of an antiferromagnetic Mott insulator via interfacial metal-insulator transitions

Received: 16 July 2024

Accepted: 4 April 2025

Published online: 15 April 2025

Check for updates

Sujan Shrestha[1], Maryam Souri[1], Christopher J. Dietl[2], Ekaterina M. Pärschke[3], Maximilian Krautloher[4], Gabriel A. Calderon Ortiz[5], Matteo Minola[4], Xiatong Shi[4], Alexander V. Boris[4], Jinwoo Hwang[5], Giniyat Khaliullin[4], Gang Cao[6], Bernhard Keimer[4], Jong-Woo Kim[2], Jungho Kim[2] & Ambrose Seo[1]

Antiferromagnetic insulators present a promising alternative to ferromagnets due to their ultrafast spin dynamics essential for low-energy terahertz spintronic device applications. Magnons, i.e., quantized spin waves capable of transmitting information through excitations, serve as a key functional element in this paradigm. However, identifying external mechanisms to effectively tune magnon properties has remained a major challenge. Here we demonstrate that interfacial metal-insulator transitions offer an effective method for controlling the magnons of Sr_2IrO_4, a strongly spin-orbit coupled antiferromagnetic Mott insulator. Resonant inelastic x-ray scattering experiments reveal a significant softening of zone-boundary magnon energies in Sr_2IrO_4 films epitaxially interfaced with metallic 4*d* transition-metal oxides. Therefore, the magnon dispersion of Sr_2IrO_4 can be tuned by metal-insulator transitions of the 4*d* transition-metal oxides. We tentatively attribute this nontrivial behavior to a long-range phenomenon mediated by magnon-acoustic phonon interactions. Our experimental findings introduce a strategy for controlling magnons and underscore the need for further theoretical studies to better understand the underlying microscopic interactions between magnons and phonons.

Magnons, i.e., collective spin wave excitations originating from spin precession in magnetically ordered materials, have the potential to serve as a promising medium for quantum information devices. Since the propagation of magnons does not require the transport of a charge, preventing electrical losses such as Joule heating[1], it gives rise to a burgeoning research field known as magnonics[2,3]. Antiferromagnetic insulators have garnered considerable attention in this emerging field, primarily due to their ultrafast spin dynamics compared to ferromagnetic counterparts, which are essential for device operation in the terahertz range[4–6]. Nevertheless, effectively guiding and coherently manipulating magnons using external stimuli is still a significant challenge.

Heterointerfaces between two different materials can provide model systems for investigating the relation between external stimuli and collective spin waves. Examples are the effects of lattice strain[7], interfacial coupling, and charge transfer on magnons[8,9] and their spin

[1]Department of Physics and Astronomy, University of Kentucky, Lexington, KY, USA. [2]Advanced Photon Source, Argonne National Laboratory, Argonne, IL, USA. [3]Department of Physics, University of Alabama at Birmingham, Birmingham, AL, USA. [4]Max-Planck-Institut für Festkörperforschung, Stuttgart, Germany. [5]Department of Materials Science and Engineering, The Ohio State University, Columbus, OH, USA. [6]Department of Physics, University of Colorado at Boulder, Boulder, CO, USA. e-mail: a.seo@uky.edu

currents[10–12]. In particular, interfaces between an antiferromagnetic insulator and a metal have been considered for novel spin-charge conversion[13,14]. Despite some astonishing predictions from magnetic insulator/metal interfaces[15], the fundamental understanding of how a metallic interface affects the spin-wave dispersion of an antiferromagnetic insulator remains elusive.

Sr_2IrO_4, a 5*d* transition-metal oxide, is a quasi-two-dimensional antiferromagnetic insulator with strong spin-orbit interaction resulting in the $J_{eff} = 1/2$ pseudospins. The distinctive canted antiferromagnetism and magnetic anisotropy in the $J_{eff} = 1/2$ state can be useful for spintronic applications[16,17]. Notably, Sr_2IrO_4 hosts spin waves at terahertz frequencies with a significant stress response mediated by strong spin-orbit interactions[7]. Its similarities to La_2CuO_4, a parent compound of high T_c superconductors, suggest a potential for superconducting antiferromagnetic magnonics[18]. Therefore, Sr_2IrO_4 presents a compelling avenue for studying the influence of metallic interfaces on spin-wave dispersion and its heterostructures offer opportunities to explore intriguing phenomena[19,20].

In this article, we report a systematic investigation of the spin-wave dispersion in Sr_2IrO_4 thin films epitaxially interfaced with various metallic and insulating single crystals. High-resolution resonant inelastic x-ray scattering (RIXS) measurements reveal a significant softening of single-magnon peaks near the (π/2, π/2) zone boundary for Sr_2IrO_4 thin films interfaced with metallic crystals, without any accompanying broadening of the magnon spectrum. In contrast, the magnon spectrum of Sr_2IrO_4 thin films remains unaltered when interfaced with insulating crystals. Raman spectroscopy further corroborates these findings, as the two-magnon excitations—predominantly representing zone-boundary magnons—exhibit a consistent trend. We propose that electron-phonon interactions, occurring either at the heterointerface or within the metallic substrate, may modify the magnon dispersion in Sr_2IrO_4 thin films via long-range magnon-acoustic phonon interactions. Complementary experimental techniques, including resonant elastic x-ray scattering, optical spectroscopy, and transmission electron microscopy, indicate that conventional interfacial mechanisms such as strain, doping, and proximity effects are unlikely to account for these observations. Our findings give an insight into magnonics, leveraging metal-insulator transitions in adjacent crystals as an effective mechanism for manipulating terahertz magnon propagation.

Results

We constructed epitaxial heterostructures by depositing Sr_2IrO_4 epitaxial thin films on ruthenates single crystals (Fig. 1) using pulsed laser deposition[21,22]. To minimize the potential influence of spin-spin interactions, we selected ruthenates with paramagnetic characteristics. Sr_2RuO_4 single crystals exhibit a tetragonal crystal structure and metallic transport behavior, while $Ca_3Ru_{1.98}Ti_{0.02}O_7$ single crystals are orthorhombic and undergo a metal-insulator transition at 55 K, exhibiting metallic behavior above this temperature and insulating behavior below it[23,24]. This transition is accompanied by minor changes in the *b*- and *c*-lattice constants (Supplementary Fig. 1). To systematically investigate the strain effects, we also studied Sr_2IrO_4 thin films deposited on insulating $(LaAlO_3)_{0.3}(Sr_2TaAlO_6)_{0.7}$ (LSAT) substrates, which has a similar lattice mismatch with Sr_2IrO_4 as Sr_2RuO_4.

High-resolution *Z*-contrast scanning transmission electron microscopy of the Sr_2IrO_4/Sr_2RuO_4 heterostructure (Supplementary Fig. 2) reveals an atomically sharp heterointerface with minimal interfacial diffusion, similar to the sharp $Sr_2IrO_4/Ca_3Ru_2O_7$ (ref. 25) and $Sr_2IrO_4/Ca_3Ru_{1.98}Ti_{0.02}O_7$ heterointerfaces (Supplementary Fig. 3). Distinct x-ray (0 0 *l*)-diffraction peaks are observed for the Sr_2IrO_4 thin films as well as the Sr_2RuO_4, $Ca_3Ru_{1.98}Ti_{0.02}O_7$, and LSAT substrates, accompanied by interference fringes near the (0 0 12) peak (Supplementary Fig. 4a).

X-ray reciprocal space mapping confirms that the in-plane lattice of Sr_2IrO_4 thin films is strained to all three substrates without relaxation (Supplementary Fig. 4b, c). Notably, the Sr_2IrO_4 thin films on both Sr_2RuO_4 and LSAT experience the same amount of compressive strain of −0.51% (Supplementary Table 1). In contrast, the Sr_2IrO_4 thin film on $Ca_3Ru_{1.98}Ti_{0.02}O_7$ undergoes a more complex strain profile: −2.22% compressive strain along the *a*-axis and 0.33% tensile strain along the *b*-axis above 55 K, which increases to 2% tensile strain along the *b*-axis below 55 K (Supplementary Table 2).

In recent years, RIXS has emerged as a powerful tool for collecting momentum-resolved and element-specific insights into collective magnetic excitations, such as magnons and spin-orbit excitons, in transition metal oxides[26–29]. Figure 2a presents representative energy loss spectra of our Sr_2IrO_4/Sr_2RuO_4 heterostructure, measured with different momentum transfers in the magnetic Brillouin zone. Figure 2b provides an intensity map derived from the energy loss spectra in Fig. 2a, highlighting the key spectral features. The low-energy range (0–0.25 eV) shows a dispersive magnetic excitation (magnon), while the higher-energy range (0.30–0.90 eV) reveals a dispersive orbital excitation (spin-orbit exciton), both of which reflect the intrinsic properties of the system[18,27]. The presence of well-defined dispersive magnons and spin-orbit excitons underscores the high crystallinity of the Sr_2IrO_4/Sr_2RuO_4 heterostructure, further validating the quality of the epitaxial thin films used in this study.

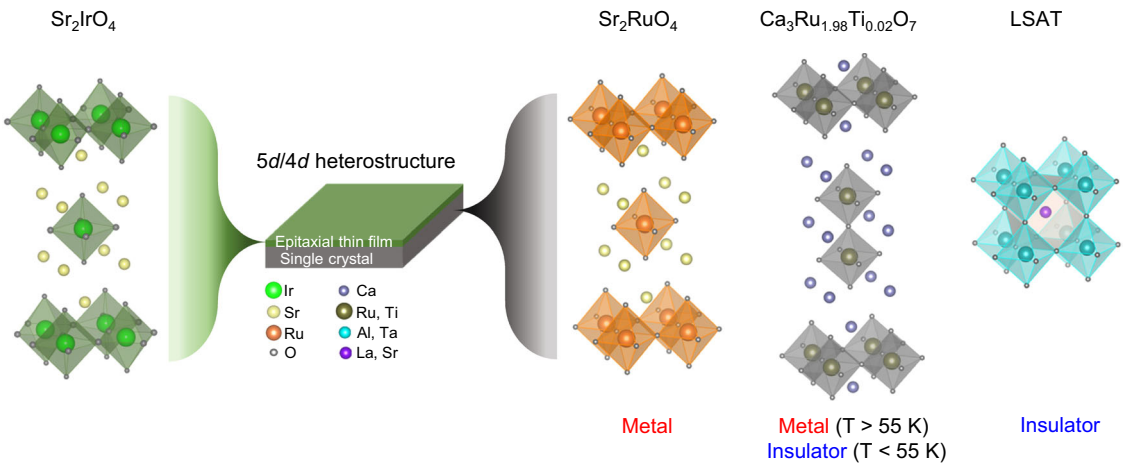

Fig. 1 | Sr_2IrO_4 thin-film heterostructure systems. Schematic representation of Sr_2IrO_4 thin films interfaced with various substrates, including ruthenates single crystals and reference LSAT substrates. Sr_2RuO_4 and LSAT single crystals have comparable in-plane lattice constants but exhibit distinct electronic properties, with Sr_2RuO_4 being metallic and LSAT insulating. The $Ca_3Ru_{1.98}Ti_{0.02}O_7$ single crystal has a temperature-dependent metal-insulator transition, exhibiting metallic behavior above 55 K and becoming insulating below this temperature.

https://doi.org/10.1038/s41467-025-58922-z

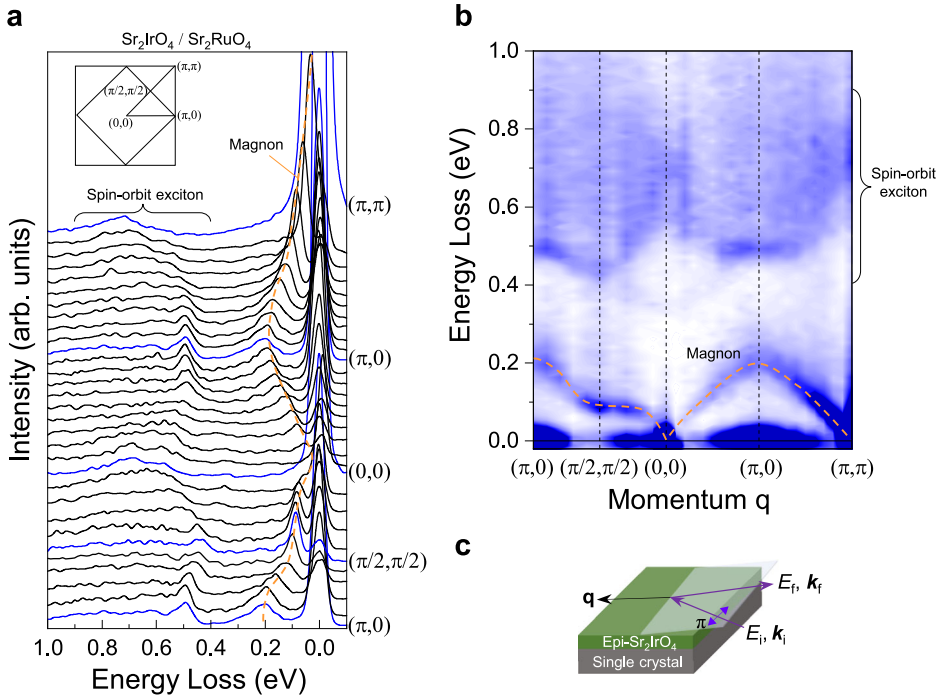

Fig. 2 | RIXS spectra of the Sr_2IrO_4/Sr_2RuO_4 heterostructure. a Energy loss spectra of the Sr_2IrO_4/Sr_2RuO_4 heterostructure at 20 K with different momenta in the Brillouin zone. The inset illustrates high symmetry points of both the undistorted tetragonal unit cell and the magnetic unit cell. **b** Image plot of the energy loss spectra shown in (**a**), highlighting the dispersive magnon and spin-orbit exciton modes. The detection of well-defined dispersive features confirms the high crystalline quality of the Sr_2IrO_4 thin film. The orange dashed line in (**a**, **b**) serves as a guide to the magnon dispersion. The intensity scale bar is in arbitrary units. **c** Schematic of the horizontal scattering geometry used during the RIXS measurements.

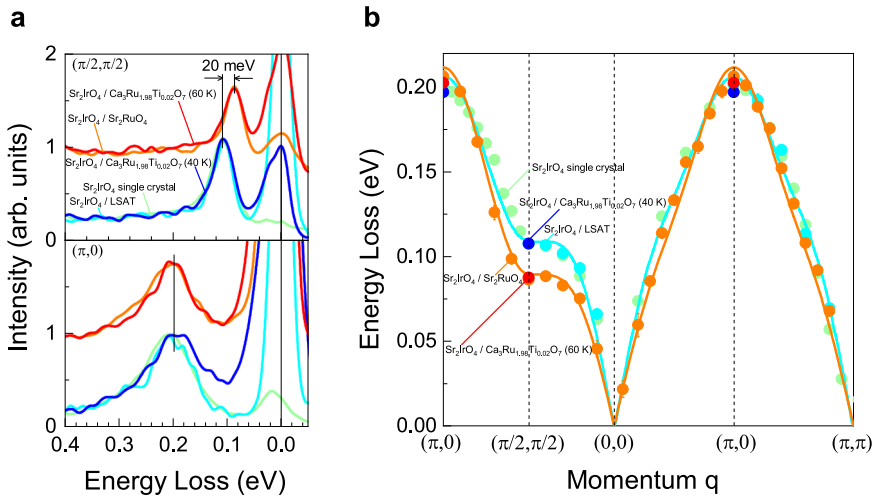

Fig. 3 | Magnon softening in Sr_2IrO_4 thin films interfaced with metallic substrates at the (π/2, π/2) zone boundary. a RIXS spectra of Sr_2IrO_4 thin films on various substrates, compared to single-crystal Sr_2IrO_4 (light green) at (π, 0) and (π/2, π/2). Substrates include metallic (Sr_2IrO_4/Sr_2RuO_4 (orange) and Sr_2IrO_4/$Ca_3Ru_{1.98}Ti_{0.02}O_7$ at T > 55 K (red)) and insulating (Sr_2IrO_4/LSAT (cyan) and Sr_2IrO_4/$Ca_3Ru_{1.98}Ti_{0.02}O_7$ at T < 55 K (blue)) crystals. Thin films interfaced with metallic substrates show pronounced softening of the single magnon mode at the (π/2, π/2) zone boundary. **b** Magnon dispersion extracted from the RIXS spectra and compared with single-crystal Sr_2IrO_4 data. The solid orange and cyan lines represent theoretical fits using the model Hamiltonian for Sr_2IrO_4/Sr_2RuO_4 and Sr_2IrO_4/LSAT, respectively.

The noteworthy feature observed in the RIXS experiments is the pronounced softening of the low-energy magnon dispersion in Sr_2IrO_4 films, specifically near the (π/2, π/2) zone boundary, when their interfaced single-crystal substrates transition from insulating to metallic states. This softening, by ~20 meV, is a striking contrast to the consistent magnon energies observed in other regions of the Brillouin zone. Figure 3a illustrates the low-energy magnon spectra of all Sr_2IrO_4 thin films along the high-symmetry directions (π, 0) and (π/2, π/2). At (π, 0), the magnon peak energy remains nearly identical, around 200 meV, across all systems studied: Sr_2IrO_4/Sr_2RuO_4, Sr_2IrO_4/$Ca_3Ru_{1.98}Ti_{0.02}O_7$ (both above and below 55 K), Sr_2IrO_4 /LSAT, and the Sr_2IrO_4 single crystal. However, at (π/2, π/2), a notable difference emerges. Thin films interfaced with metallic substrates—Sr_2IrO_4/Sr_2RuO_4 (orange) and Sr_2IrO_4/$Ca_3Ru_{1.98}Ti_{0.02}O_7$ above 55 K (red)—exhibit a significant softening of the magnon peak energy, with a reduction of approximately 20 meV. In contrast, thin films on

insulating substrates, such as $Sr_2IrO_4/Ca_3Ru_{1.98}Ti_{0.02}O_7$ below 55 K (blue) and Sr_2IrO_4/LSAT (cyan), show magnon peak energies at (π/2, π/2) that are indistinguishable from that of the Sr_2IrO_4 single crystal. This shift in magnon energy exceeds the experimental error bar, underscoring the significance of this observation[28].

Essentially, the results can be categorized into two groups (Fig. 3b): Sr_2IrO_4 heterostructures with insulating substrates retain higher magnon energy near (π/2, π/2), comparable to single-crystal Sr_2IrO_4, while those interfaced with metallic substrates exhibit a pronounced magnon energy softening, reduced by approximately 20 meV. This behavior highlights the critical role of substrate properties—particularly metallicity—in tuning the magnon dispersion of Sr_2IrO_4 thin films. The softened magnon energy at (π/2, π/2) is a highly unusual phenomenon, as it increases the magnon dispersion between the (π, 0) and (π/2, π/2) zone boundaries.

In typical antiferromagnetic $S = 1/2$ systems like La_2CuO_4, the magnon energy difference between these zone boundaries is relatively small, as observed in inelastic neutron scattering experiments[30]. However, in Sr_2IrO_4 single crystals (a $J_{eff} = 1/2$ pseudospin system), this energy difference is significantly larger, and it increases further in Sr_2IrO_4 thin films interfaced with metallic substrates. According to linear spin-wave theory[18,31], the magnon energy dispersion ($\omega_{\mathbf{q}}$) is described as: $\omega_{\mathbf{q}} = \sqrt{A_{\mathbf{q}}^2 - B_{\mathbf{q}}^2}$, where: $A_{\mathbf{q}} = 2(J_1 - J_2 - J_3 + J_2 \cos q_x \cos q_y) + J_3(\cos 2q_x + \cos 2q_y)$, $B_{\mathbf{q}} = J_1(\cos q_x + \cos q_y)$. Here, J_1, J_2, and J_3 represent the in-plane exchange interactions between the nearest, next-nearest, and third-nearest neighbors, respectively. The magnon energies at the (π, 0) and (π/2, π/2) zone boundaries are expressed as: $\omega_{(\pi,0)} = 2(J_1 - 2J_2)$, $\omega_{(\frac{\pi}{2},\frac{\pi}{2})} = 2(J_1 - J_2 - 2J_3)$. Thus, the experimentally observed magnon softening near the (π/2, π/2) zone boundary can be attributed to changes in J_2 and J_3, specifically $2(-J_2 + 2J_3)$.

By fitting the magnon dispersion data (Fig. 3b) using the Heisenberg spin model, we extracted the in-plane exchange interactions up to the fourth-nearest neighbor (J_4) for the $J_{eff} = 1/2$ pseudospins in Sr_2IrO_4. The best-fit parameters are summarized in Supplementary Table 3: For the Sr_2IrO_4 thin films contacted with insulating substrates: $J_1 = 55$ meV, $J_2 = -17$ meV, $J_3 = 16$ meV, and $J_4 = 7.3$ meV. For thin films interfaced with metallic substrates: $J_1 = 55$ meV, $J_2 = -21$ meV, $J_3 = 20$ meV, and $J_4 = 4.6$ meV. Notably, while J_1 remains unchanged, the magnitudes of J_2 and J_3 increase in Sr_2IrO_4 interfaced with metallic substrates, consistent with the predictions of linear spin-wave theory discussed above.

The two-magnon peak energies observed in high-resolution Raman spectra corroborate the RIXS results. Figure 4a illustrates the B_{2g} two-magnon modes in Sr_2IrO_4/Sr_2RuO_4 and Sr_2IrO_4/LSAT at 10 K, while Fig. 4b presents the temperature-dependent Raman spectra of B_{2g} two-magnon modes in $Sr_2IrO_4/Ca_3Ru_{1.98}Ti_{0.02}O_7$. The two-magnon peak energies (ω_{2M}) were determined by fitting the data to a model function comprising two Lorentz oscillators. Notably, the two-magnon energies of thin films on metallic substrates (Sr_2RuO_4 and $Ca_3Ru_{1.98}Ti_{0.02}O_7$ above 55 K) are lower than those of thin films on insulating substrates ($Ca_3Ru_{1.98}Ti_{0.02}O_7$ below 55 K and LSAT). Given that the two-magnon mode primarily reflects zone boundary excitations[32], this observation is consistent with the softening of the (π/2, π/2) zone boundary magnon. These results establish a strong agreement between the Raman and RIXS measurements, further confirming the substrate-dependent modification of magnon dynamics in Sr_2IrO_4 thin films.

Raman spectroscopy reveals a noticeable hardening of the phonon modes in Sr_2IrO_4 thin films by ~8–11 cm^{-1} (1–1.4 meV) when the contacted substrate transitions from insulating to metallic, likely indicating electron-phonon interactions. Figure 5a shows the A_{1g} and B_{2g} phonon modes of the Sr_2IrO_4 thin film in the Sr_2IrO_4/LSAT and Sr_2IrO_4/Sr_2RuO_4 heterostructures. While the phonon modes in

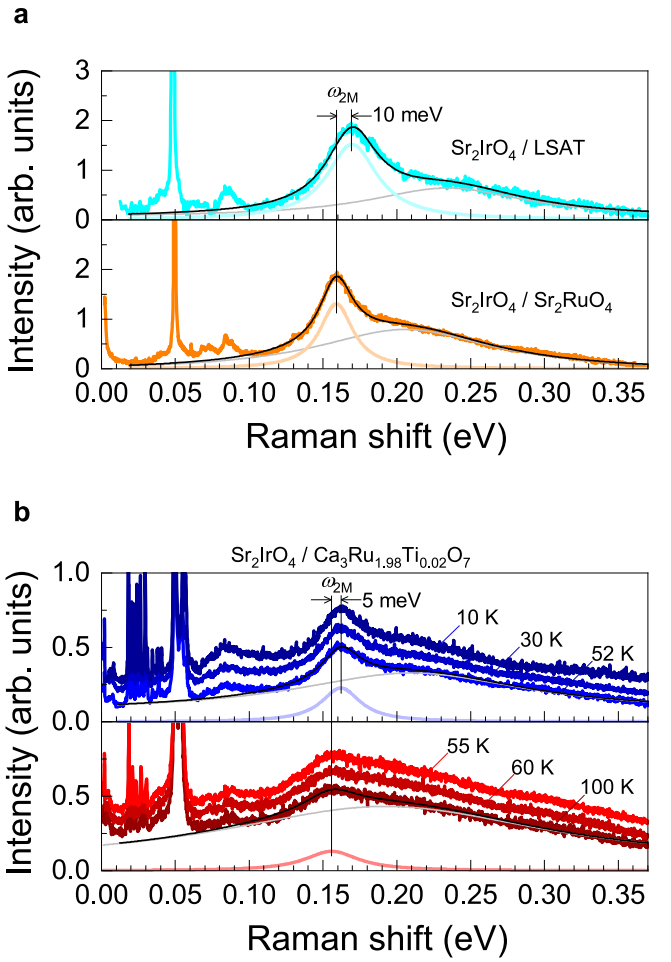

Fig. 4 | Softening of two-magnon modes in Sr_2IrO_4 thin films interfaced with metallic substrates. a Raman spectra of B_{2g} two-magnon modes in Sr_2IrO_4/Sr_2RuO_4 (orange) and Sr_2IrO_4/LSAT (cyan) heterostructures measured at 10 K. **b** Temperature-dependent Raman spectra of B_{2g} two-magnon modes in the $Sr_2IrO_4/Ca_3Ru_{1.98}Ti_{0.02}O_7$ heterostructure. The two-magnon peak energy is lower in Sr_2IrO_4 thin films interfaced with metallic substrates (Sr_2RuO_4 and $Ca_3Ru_{1.98}Ti_{0.02}O_7$ at $T > 55$ K) compared to those interfaced with insulating substrates (LSAT and $Ca_3Ru_{1.98}Ti_{0.02}O_7$ at $T < 55$ K). Two-magnon peak positions in both figures were determined using fits to a model comprising two Lorentz oscillators, represented by smooth solid curves for each component. The total fit is shown by the black solid line.

Sr_2IrO_4/LSAT closely resemble those of Sr_2IrO_4 single crystals, the Sr_2IrO_4/Sr_2RuO_4 heterostructure exhibits a significant upward energy shift of approximately 1.4 meV for the A_{1g} mode and 1 meV for the B_{2g} mode. Similarly, an upward shift of up to 0.7 meV in phonon energy is observed in $Sr_2IrO_4/Ca_3Ru_{1.98}Ti_{0.02}O_7$ heterostructures when the substrate transitions from an insulating to a metallic state at 55 K (Fig. 5b).

It is important to note that the structural change occurring in the $Ca_3Ru_{1.98}Ti_{0.02}O_7$ substrate at 55 K may also contribute to the observed phonon mode shift in $Sr_2IrO_4/Ca_3Ru_{1.98}Ti_{0.02}O_7$ heterostructures. Additionally, we investigated other heterostructures, including $Sr_2IrO_4/Ca_2Ru_{0.91}Mn_{0.09}O_4$ (insulator), Sr_2IrO_4/Sr_2RhO_4 (metal), and $Sr_2IrO_4/Ca_3Ru_2O_7$ (metal) at 10 K. These heterostructures exhibited a similar trend: the metallic substrates induced hardening of the B_{2g} phonons in the Sr_2IrO_4 thin films by about 8 cm^{-1} (1 meV) compared to insulating substrates (Supplementary Fig. 5). Overall, a common factor across all results is the metallic state of the substrate, which strongly correlates with the observed phonon mode stiffening in Sr_2IrO_4 thin films.

https://doi.org/10.1038/s41467-025-58922-z

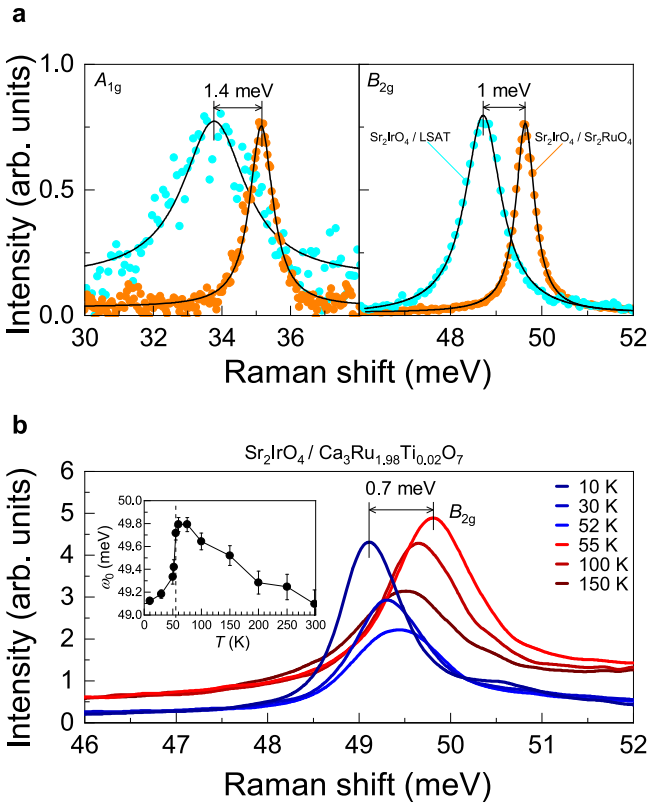

Fig. 5 | Hardening of phonons in Sr_2IrO_4 interfaced with metallic substrates. **a** A_{1g} and B_{2g} phonon modes of Sr_2IrO_4/Sr_2RuO_4 (orange) and Sr_2IrO_4/LSAT (cyan) heterostructures. The solid black lines represent Lorentzian fits to the data. **b** Temperature-dependent evolution of the B_{2g} phonon modes in the Sr_2IrO_4/$Ca_3Ru_{1.98}Ti_{0.02}O_7$ heterostructure. Inset: Temperature-dependent peak position of the B_{2g} phonon modes in the same heterostructure, illustrating the phonon hardening behavior as the substrate transitions from an insulating to a metallic state. Error bars represent uncertainties estimated from the peak widths and curve-fits.

Discussion

Our observations of significant magnon softening and phonon mode hardening in Sr_2IrO_4 thin films interfaced with metallic substrates, compared to insulating substrates, offer valuable insights into the underlying coupling mechanisms. However, the change in phonon energies ($\Delta\omega_{phonon}$) is an order of magnitude smaller than the change in magnon energies ($\Delta\omega_{magnon}$). Reconciling the relatively small (~1 meV) phonon shifts with the much larger (~20 meV) magnon energy changes is challenging. Instead, these phonon shifts likely originate from structural distortions associated with the metal-insulator transition, as their magnitudes are comparable to shifts induced by thermal effects.

Developing a microscopic, quantitative theory for electron-phonon-magnon couplings in such complex heterostructures is beyond the scope of this work. The form of the magnon-phonon (or spin-phonon) Hamiltonian is inherently complex, as lattice vibrations break lattice symmetries, introducing anisotropic magnetic interaction terms even in two-dimensional systems. Consequently, first-principle calculations of all magnon-phonon coupling parameters are practically infeasible.

Nevertheless, to explain the observed modifications in magnetic interactions across the tens-of-nanometer-thick Sr_2IrO_4 thin film, we propose a mechanism involving propagating longitudinal acoustic phonons. These phonons, sensitive to substrate charge carriers due to metallic screening effects, mediate long-range spin interactions through magnetoelastic coupling. This coupling, particularly pronounced in spin-orbit entangled magnets like Sr_2IrO_4, arises from the direct interaction of lattice vibrations with the unquenched orbital components of the magnetic moments. Magnetoelastic interactions effectively generate spin-spin couplings mediated by dispersive phonon modes, extending beyond nearest neighbors. As metallic screening softens the acoustic phonons, the resulting enhancement in phonon-mediated spin interactions aligns with the increased J_2 and J_3 values—while J_1 remains constant—as deduced from our phenomenological fits (Fig. 3b) and linear spin-wave theory.

Similar effects have been observed in lightly doped Sr_2IrO_4, where magnon softening and anisotropic momentum-space behavior were attributed to enhanced longer-range spin couplings mediated by softened phonons[33]. However, unlike the doped case, our heterostructures exhibit no broadening of magnon peaks or collapse of long-range magnetic order, suggesting that the observed changes are driven by indirect acoustic phonon-mediated interactions rather than direct coupling between Ir magnetic moments and substrate conduction electrons.

Alternative mechanisms, such as lattice strain, interfacial proximity effects, or charge transfer, are insufficient to explain the observed phenomena. The strain effect, for example, fails to account for magnon softening in Sr_2IrO_4/Sr_2RuO_4 heterostructures, as similar strain states in Sr_2IrO_4/LSAT heterostructures do not show comparable effects. Proximity effects at the interface are also unlikely, as our observations are made through bulk-sensitive techniques[26]. These experimental techniques probe the entire volume of the 20–50 nm (30-80 IrO_2 layers) thin films, rather than being confined to the interface region. Moreover, Sr_2IrO_4/Sr_2RuO_4 heterostructures of varying thicknesses (12, 30, and 50 nm) show consistent magnon softening without a noticeable thickness dependence (Supplementary Fig. 6), indicating that the observed behavior is a long-range effect throughout the thin film.

Charge transfer as a mechanism also fails to explain the results. If charge transfer at the interface involved hole doping, it would typically harden the magnon peak energy at the zone boundary[34,35], contrary to our observations. On the other hand, electron doping is known to soften the magnon peak energy but often results in significant broadening of the magnon spectrum and a collapse of long-range magnetic order in Sr_2IrO_4 (refs. 33,36.). In both Sr_2IrO_4/$Ca_3Ru_{1.98}Ti_{0.02}O_7$ and Sr_2IrO_4/Sr_2RuO_4 heterostructures, however, no broadening of magnon peaks (Fig. 3a) or collapse of long-range magnetic order was observed (Supplementary Fig. 7).

Resonant x-ray scattering near the Ru L_2 edge further confirms the absence of Ru ions in the Sr_2IrO_4 thin film (Supplementary Fig. 8), ruling out intermixing between Ir and Ru ions. Additionally, optical spectroscopy reveals a clear insulating gap of approximately 0.3 eV in the Sr_2IrO_4/Sr_2RuO_4 heterostructure (Supplementary Fig. 9), similar to that of Sr_2IrO_4 single crystals, further eliminating charge transfer as a plausible explanation for the observed phenomena.

In summary, we have observed a pronounced softening of the zone boundary magnon energy when Sr_2IrO_4 thin films are epitaxially interfaced with metallic 4*d* TMO single crystals. We propose that electron-phonon coupling, occurring either at the interface or within the metallic substrate, influences the magnon dispersion in Sr_2IrO_4 via a long-range magnon-acoustic phonon interaction. This mechanism enhances second- and third-nearest-neighbor interactions, while its impact on the nearest-neighbor exchange remains minimal. Our findings underscore the need for further theoretical studies and calculations to develop a deeper understanding of the microscopic interactions between magnons and phonons in such complex systems.

In addition to the well-established role of acoustic waves in mediating magnon-phonon coupling[37], we propose that metal-insulator transitions at heterointerfaces represent an effective mechanism for tuning magnons—an essential requirement for advancing magnonics. Our study also raises several compelling questions and broader perspectives. For instance, is this phenomenon unique to 5*d*/4*d* TMO heterostructures, or could it be extended to other

magnetic systems, such as Yttrium iron garnets[38] or van der Waals heterostructures incorporating two-dimensional magnets like Fe_3GeTe_2, $NiPS_3$, CrSBr, where strong magnon-exciton coupling[39] has already been observed? Future investigations across a broader range of heterostructures, featuring diverse materials and magnetic systems, will be essential for addressing these questions and further unraveling the fundamental interactions governing spin excitations in complex quantum systems.

Methods

Sample synthesis

The 5*d*/4*d* epitaxial heterostructures were fabricated by depositing Sr_2IrO_4 epitaxial thin films on ruthenates single crystals using a custom-built pulsed laser deposition system[40]. The growth conditions are a laser fluence of 1.2 J/cm^2, a substrate temperature of 700 °C, and an oxygen partial pressure of 10 mTorr. The thicknesses of the Sr_2IrO_4 thin films were determined to be ~12 nm, 30 nm, 50 nm (Sr_2IrO_4/Sr_2RuO_4), 50 nm (Sr_2IrO_4/LSAT), and 20 nm ($Sr_2IrO_4/Ca_3Ru_{1.98}Ti_{0.02}O_7$).

X-ray scattering experiments

High-resolution x-ray diffraction and RIXS experiments were conducted at the 6-ID-B beamline and the 27-ID beamline of the Advanced Photon Source, Argonne National Laboratory, respectively. For RIXS spectra, a horizontal scattering geometry was employed with incident x-ray photons tuned to the Ir L_3 edge ($\hbar\omega = 11217$ eV) and polarized in the π-direction, as illustrated in Fig. 2c.

Scanning transmission electron microscopy

Cross-sectional specimens for high-resolution scanning transmission electron microscopy were prepared using a Thermofisher Helios focused ion beam with a gallium ion source. These specimens underwent additional cleaning via argon ion milling (Fichicone Nanomill) at a beam energy of 500 eV to eliminate amorphous layers. Transmission electron microscopy images were captured with a Thermofisher Titan operating at 300 kV and employing a collection angle range of 80–300 milliradians.

Raman spectroscopy

Temperature-dependent Raman spectra were obtained in back-scattering geometry using a Jobin Yvon LabRAM HR800 spectrometer equipped with a confocal microscope. A 1.96 eV excitation line from a helium-neon laser was used, producing a focused beam spot with a diameter of ~5 µm.

Optical spectroscopy

The optical conductivity spectrum was measured using a home-built ellipsometer attached to a Bruker 66 V FT-IR spectrometer and an M2000 ellipsometer (Woollam) for the spectral ranges of 0.05–1.0 eV and 1.2–6 eV, respectively.

Data availability

All the data used to generate figures are provided with this paper in the Source Data file. Additional data related to this paper may be requested from the corresponding author. Source data are provided with this paper.

References

1. Grundler, D. Reconfigurable magnonics heats up. *Nat. Phys.* **11**, 438–441 (2015).
2. Kruglyak, V. V., Demokritov, S. O. & Grundler, D. Magnonics. *J. Phys. D: Appl. Phys.* **43**, 264001 (2010).
3. Lenk, B., Ulrichs, H., Garbs, F. & Münzenberg, M. The building blocks of magnonics. *Phys. Rep.* **507**, 107–136 (2011).
4. Baltz, V. et al. Antiferromagnetic spintronics. *Rev. Mod. Phys.* **90**, 015005 (2018).
5. Jungwirth, T., Marti, X., Wadley, P. & Wunderlich, J. Antiferromagnetic spintronics. *Nat. Nanotechnol.* **11**, 231–241 (2016).
6. Rezende, S. M., Azevedo, A. & Rodríguez-Suárez, R. L. Introduction to antiferromagnetic magnons. *J. Appl. Phys.* **126**, 151101 (2019).
7. Kim, H.-H. et al. Giant stress response of terahertz magnons in a spin-orbit Mott insulator. *Nat. Commun.* **13**, 6674 (2022).
8. Meng, Y. et al. Direct evidence of antiferromagnetic exchange interaction in Fe(001) films: Strong magnon softening at the high-symmetry M point. *Phys. Rev. B* **90**, 174437 (2014).
9. Chuang, T. H. et al. Magnetic properties and magnon excitations in Fe(001) films grown on Ir(001). *Phys. Rev. B* **89**, 174404 (2014).
10. Zhou, Y. et al. Piezoelectric strain-controlled magnon spin current transport in an antiferromagnet. *Nano Lett.* **22**, 4646–4653 (2022).
11. Liang, Y. et al. Observation of magnon spin transport in $BiFeO_3$ thin films. *Adv. Funct. Mater.* **34**, 2308944 (2024).
12. Li, J. et al. Spin current from sub-terahertz-generated antiferromagnetic magnons. *Nature* **578**, 70–74 (2020).
13. Rongione, E. et al. Emission of coherent THz magnons in an antiferromagnetic insulator triggered by ultrafast spin–phonon interactions. *Nat. Commun.* **14**, 1818 (2023).
14. Kholid, F. N. et al. The importance of the interface for picosecond spin pumping in antiferromagnet-heavy metal heterostructures. *Nat. Commun.* **14**, 538 (2023).
15. Fjærbu, E. L., Rohling, N. & Brataas, A. Superconductivity at metal-antiferromagnetic insulator interfaces. *Phys. Rev. B* **100**, 125432 (2019).
16. Lee, N. et al. Antiferromagnet-Based spintronic functionality by controlling isospin domains in a layered perovskite iridate. *Adv. Mater.* **30**, 1805564 (2018).
17. Wang, H. et al. Giant anisotropic magnetoresistance and non-volatile memory in canted antiferromagnet Sr_2IrO_4. *Nat. Commun.* **10**, 2280 (2019).
18. Kim, J. et al. Magnetic excitation spectra of Sr_2IrO_4 probed by resonant inelastic x-ray scattering: establishing links to cuprate superconductors. *Phys. Rev. Lett.* **108**, 177003 (2012).
19. Meng, K.-Y. et al. Observation of nanoscale skyrmions in $SrIrO_3$/$SrRuO_3$ bilayers. *Nano Lett.* **19**, 3169–3175 (2019).
20. Matsuno, J. et al. Interface-driven topological Hall effect in $SrRuO_3$-$SrIrO_3$ bilayer. *Sci. Adv.* **2**, e1600304 (2016).
21. Nichols, J. et al. Tuning electronic structure via epitaxial strain in Sr_2IrO_4 thin films. *Appl. Phys. Lett.* **102**, 141908 (2013).
22. Seo, S. S. A. et al. Selective growth of epitaxial Sr_2IrO_4 by controlling plume dimensions in pulsed laser deposition. *Appl. Phys. Lett.* **109**, 201901 (2016).
23. Krautloher, M. *Neutron scattering studies on layered ruthenates*. PhD thesis, University of Stuttgart (2018).
24. Rabinovich, K. S. et al. Optically driven dynamics of a mott insulator-to-metal transition. *Adv. Funct. Mater.* **35**, 2416597 (2025).
25. Shrestha, S. et al. Emergent interlayer magnetic order via strain-induced orthorhombic distortion in the 5*d* Mott insulator Sr_2IrO_4. *Phys. Rev. B* **105**, L100404 (2022).
26. Ament, L. J. P., van Veenendaal, M., Devereaux, T. P., Hill, J. P. & van den Brink, J. Resonant inelastic x-ray scattering studies of elementary excitations. *Rev. Mod. Phys.* **83**, 705–767 (2011).
27. Kim, J. et al. Excitonic quasiparticles in a spin–orbit Mott insulator. *Nat. Commun.* **5**, 4453 (2014).
28. Kim, J. et al. Quartz-based flat-crystal resonant inelastic x-ray scattering spectrometer with sub-10 meV energy resolution. *Sci. Rep.* **8**, 1958 (2018).
29. Paris, E. et al. Strain engineering of the charge and spin-orbital interactions in Sr_2IrO_4. *Proc. Natl. Acad. Sci. USA* **117**, 24764–24770 (2020).
30. Coldea, R. et al. Spin waves and electronic interactions in La_2CuO_4. *Phys. Rev. Lett.* **86**, 5377–5380 (2001).

31. Schmitt-Rink, S., Varma, C. M. & Ruckenstein, A. E. Spectral function of holes in a quantum antiferromagnet. *Phys. Rev. Lett.* **60**, 2793–2796 (1988).
32. Fleury, P. A. & Loudon, R. Scattering of light by one- and two-magnon excitations. *Phys. Rev.* **166**, 514–530 (1968).
33. Gretarsson, H. et al. Persistent paramagnons deep in the metallic phase of $Sr_{2-x}La_xIrO_4$. *Phys. Rev. Lett.* **117**, 107001 (2016).
34. Zhong, Z. & Hansmann, P. Band alignment and charge transfer in complex oxide interfaces. *Phys. Rev. X* **7**, 011023 (2017).
35. Bertinshaw, J. et al. Spin-wave gap collapse in Rh-doped Sr_2IrO_4. *Phys. Rev. B* **101**, 094428 (2020).
36. Liu, X. et al. Anisotropic softening of magnetic excitations in lightly electron-doped Sr_2IrO_4. *Phys. Rev. B* **93**, 241102 (2016).
37. Lyons, T. P. et al. Acoustically driven magnon-phonon coupling in a layered antiferromagnet. *Phys. Rev. Lett.* **131**, 196701 (2023).
38. Princep, A. J. et al. The full magnon spectrum of yttrium iron garnet. *npj Quantum Mater.* **2**, 63 (2017).
39. Bae, Y. J. et al. Exciton-coupled coherent magnons in a 2D semiconductor. *Nature* **609**, 282–286 (2022).
40. Gruenewald, J. H., Nichols, J. & Seo, S. S. A. Pulsed laser deposition with simultaneous in situ real-time monitoring of optical spectroscopic ellipsometry and reflection high-energy electron diffraction. *Rev. Sci. Instrum.* **84**, 043902 (2013).

Acknowledgements

We acknowledge the support of National Science Foundation Grant No. DMR–2104296 for sample synthesis and characterization. This research used resources of the Advanced Photon Source; a U.S. Department of Energy (DOE) Office of Science user facility operated for the DOE Office of Science by Argonne National Laboratory under Contract No. DE-AC02-06CH11357. Electron microscopy was performed at the Center for Electron Microscopy and Analysis at the Ohio State University supported by National Science Foundation Grant No. DMR–1847964. G.C. acknowledges NSF support via Grant No. DMR 2204811. We acknowledge support from the European Research Council under Advanced Grant No. 101141844 (SpecTera) and the Deutsche Forschungsgemeinschaft (DFG, German Research Foundation) through Project No. 107745057-TRR 80.

Author contributions

S.S., M.S., and A.S. fabricated the heterostructures. S.S., C.D., A.S., J.-W.K., and J.K. performed synchrotron x-ray experiments and data analysis. M.K., B.K., and G.C. synthesized ruthenate single crystals. A.S. and M.M. performed Raman spectroscopy and data analysis. G.A.C.O. and J. H. performed transmission electron microscopy. X.S., A.S., and A.V.B. performed infrared spectroscopy. E.M.P., G.K., and B.K. contributed to the theoretical calculations and insights. A.S. designed the project. S.S., M.S., and A.S. wrote the manuscript with all authors' input.

Competing interests

The authors declare no competing interests.

Additional information

Supplementary information The online version contains supplementary material available at https://doi.org/10.1038/s41467-025-58922-z.

Correspondence and requests for materials should be addressed to Ambrose Seo.

Peer review information *Nature Communications* thanks the anonymous reviewer(s) for their contribution to the peer review of this work. A peer review file is available.